TASK QUARTERLY 8 No 1 (2004), 27–40

THREE-DIMENSIONAL NUMERICAL ANALYSIS OF INTERNAL FLOW PHENOMENA IN A DIAGONAL ROTOR

YOU BIN AND WU KEQI

School of Energy and Power Engineering,
Huazhong University of Science & Technology,
Wuhan, Hubei, 430074, P. R. China
youbinldy@hotmail.com

(Received 29 January 2003; revised manuscript received 28 October 2003)

Abstract: A numerical analysis has been designed to study internal flow phenomena in a diagonal rotor. A calculated diagonal rotor was designed by a quasi-three-dimensional method. Its hub and casing walls were inclined 45° and 25°, respectively. The numerical simulation was based on the Navier-Stokes equations coupled with a k-ε turbulence model. We found that the rotor's wake was stronger near the hub and in the casing end wall region. The wake at a lower flow rate was stronger than that at a higher flow rate. Static pressure gradually increased from the hub to the casing along the height of a blade, on the rotor pressure surface and in the front 60% of the chord region of the suction surface. In the back 40% of the chord region of the suction surface, static pressure gradually decreased. A passage vortex formed in the stator flow passage and an 80% axial chord plane. It was located near the hub end-wall. The passage vortex developed into a large vortex centered near the midspan at a 99% axial chord plane of the stator. The casing wall boundary layer downstream of the rotor occupied approximately 10% of the flow passage. Along the height of a blade, the meridian velocity gradually increased upstream of rotor and decreased downstream. The calculated aerodynamic characteristic curve, the meridian velocity distribution upstream and downstream of the rotor, and the streamline distribution on the meridian surface were consistent with experimental results and design data. Our findings proved that the present numerical method is reliable and practicable. It can be used to design and analyze swept diagonal rotors in order to improve their surging and rotation stall state. The present results also provide comparative data for the design of highly-loaded swept diagonal rotors in future studies.

Keywords: diagonal rotor, numerical analysis, internal flow, three-dimensional analysis

Nomenclature

φ – the flow coefficient,
ψ – the total pressure rise coefficient,
Q – the volume flow rate,
ΔP – total pressure rise,
U_t – tangential velocity at the rotor exit,
ρ – density,
D_t – tip diameter at the rotor exit,

v – the hub/tip ratio,
U_i, U_j – mean velocity components,
P_t – total pressure,
P_{st} – static pressure,
z – axial direction,
Cm – meridian velocity,
Cz – axial velocity,
ω – angular velocity of the rotor,
η – the total pressure efficiency,
X_i, X_j – Cartesian coordinates,
K – kinetic energy of turbulence,
ε – dissipation rate,
μ – dynamic viscosity,
μ_t – turbulent (or eddy) viscosity,
SCM – the streamline curvature method,
P – pressure,
R – radius of the rotor,
r_h – radius of the rotor hub,
r_c – radius of the rotor casing,
c – chord length of the rotor,
P.S – pressure surface,
S.S – suction surface,
Surf. – surface.

Definitions

$$U_t = 0.5\, D_t \omega,$$
$$\varphi = \frac{Q}{\pi D_t^2 (1-v^2) U_t/4},$$
$$\psi = \frac{\Delta P}{\frac{1}{2}\rho U_t^2}.$$

1. Introduction

Swept and skewed impellers have been successful applied in aeroengines [1–4]. Turbomachinery researchers have begun to design swept and skewed diagonal rotors for the purpose of improving surge and rotation stall state. In order to design an appropriate skewed diagonal rotor with high performance, complex internal flow details such as the end-wall boundary layer, rotor wake, passage vortex, and pressure distribution on the rotor's/stator's surface, *etc.* must be understood [5]. Due to limitations in measurement apparatus and methods, it is difficult to capture complex flow phenomena under experimental conditions. A limited amount of data is available on numerical analysis of flow phenomena in diagonal rotors.

In order to (i) gain a better understanding of the internal flow details in diagonal rotors, (ii) validate the reliability and practicality of the current numerical methods and quasi-three-dimensional methods and (iii) provide comparative results for the design of highly-loaded swept diagonal rotor in future studies, this paper analyzes flow phenomena in a diagonal rotor by solving the Navier-Stokes viscous differential equations.

2. Fan geometry and design specifications

The diagonal rotor analyzed in this study is widely used in engineering. It was designed by the modified quasi three-dimensional method. The design format utilized a streamline curvature to determine the average stream surface by solving the meridian through flow. The stream surface was transformed into a two dimensional plane to select the blade elements by using experimental cascade data. To account for the effects due to the stream surface's inclination and variations in its thickness, the cascade geometries were theoretically corrected by using Schlichting's singularity method [6–8].

The rotor shapes of the hub and the casing walls were cones with inclinations of 45° and 25°, respectively. The design vortex of the rotor was a free vortex with axial inlet condition. The diagonal rotor geometry profile is shown in Figure 1. Its basic geometric specifications are given in Table 1.

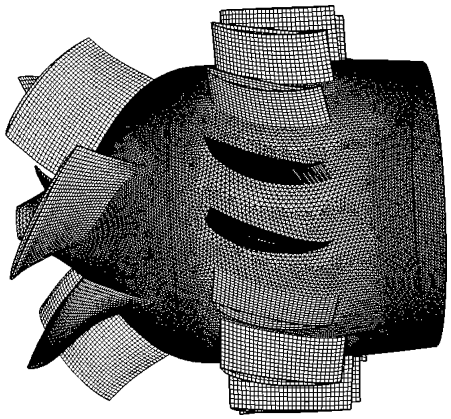

Figure 1. A profile of the diagonal rotor's geometry

Table 1. Geometry specifications of the diagonal rotor

	Rotor (hub to tip)	Stator (hub to tip)
Vortex Design	Free Vortex	Free Vortex
Number of Blades	6	15
Blade Profile	Naca65	Naca65
Blade thickness (τ)	10% to 4%	8%
Tip Diameter (D_t)	0.400m	0.450m
Hub-tip Ratio (v)	0.75 (Rotor Exit)	0.73
Solidity at tip (σ)	1.481 to 1.054	2.053 to 1.434
Camber (C_{10})	1.755 to 0.821	2.021 to 1.887
Stagger angle (β_A)	34.47° to 57.84°	17.58° to 15.62°

3. Numerical methods

In the present study, the flow is regarded as steady. The code solves the Reynolds-averaged Navier-Stokes viscous differential equations. The code is fully three-dimensional and employs a finite volume method. The turbulence is modeled according to the standard k-ε turbulence model. In the wall regions, the model uses

standard wall functions. The governing equations written in a highly conserved form are as follows:

- the continuity equation is:

$$\frac{\partial}{\partial x_i}(\rho u_i) = 0, \tag{1}$$

- while the momentum equation is:

$$\frac{\partial}{\partial x_j}(\rho u_i u_j) + \frac{\partial P}{\partial x_i} - \frac{\partial}{\partial x_j}\left(\mu\left(\frac{\partial u_i}{\partial x_j} + \frac{\partial u_j}{\partial x_i}\right)\right) = S_{ui}, \tag{2}$$

where S is the source term, and represents the Coriolis force and the centrifugal force.

The kinetic energy of turbulence, k, and its dissipation rate, ε, are obtained from the following transport equations:

$$\rho u_i \frac{\partial K}{\partial x_i} = \frac{\partial}{\partial x_i}\left[\left(\mu + \frac{\mu_t}{\sigma_k}\right)\frac{\partial K}{\partial x_i}\right] + \mu_t \frac{\partial u_i}{\partial x_j}\left(\frac{\partial u_i}{\partial x_j} + \frac{\partial u_j}{\partial x_i}\right) - \rho\varepsilon, \tag{3}$$

$$\rho u_i \frac{\partial \varepsilon}{\partial x_i} = \frac{\partial}{\partial x_i}\left[\left(\mu + \frac{\mu_t}{\sigma_k}\right)\frac{\partial \varepsilon}{\partial x_i}\right] + \frac{C_1\varepsilon}{k}\mu_t \frac{\partial u_i}{\partial x_j}\left(\frac{\partial u_i}{\partial x_j} + \frac{\partial u_j}{\partial x_i}\right) - C_2\rho\frac{\varepsilon^2}{K}. \tag{4}$$

The turbulence (or eddy) viscosity, μ_t, is computed by combining k and ε as follows:

$$\mu_t = \rho C_\mu \frac{K^2}{\varepsilon}, \tag{5}$$

where C_1, C_2, and C_μ are constants with the following values: $C_1 = 1.44$, $C_2 = 1.92$, $C_\mu = 0.09$. The standard wall functions are adopted, and the law of the wall for mean velocity meets the following equation:

$$U^* = \frac{1}{k_v}\ln\left(E\ \frac{\rho C_\mu^{1/4} k_p^{1/2} y_p}{\mu}\right), \tag{6}$$

where $k_v = 0.42$ is von Karman's constant; $E = 9.81$, is an empirical constant; K_p is the kinetic energy of turbulence at point p; y_p is the distance from point P to the wall; and μ is the dynamic viscosity of the fluid at point p.

The above equations were solved with an implicit segregated solver algorithm. As shown in Figure 2, this algorithm is based on solving the governing equations sequentially (segregated from one another). The momentum, turbulence kinetic energy and turbulence dissipation rate equations are discretized using a second-order upwind scheme. In order to satisfy the mass and momentum conservation laws, pressure and velocity are coupled by SIMPLE [9, 10] method. The flow is regarded as converged when the maximum of all normalized residues is less than $1 \cdot 10^{-5}$.

4. Computational domain and grid generation

The tip clearance is omitted in the calculation because of the large number of nodes necessary to fully resolve the flow in the tip region has overwhelmed the available computing resources. It has been assumed that the tip clearance can be neglected for moderately loaded blades without severely affecting the flow.

According to the engineering configuration of the diagonal rotor, the computational domain has been selected from 242.5 mm upstream of the rotor's leading edge

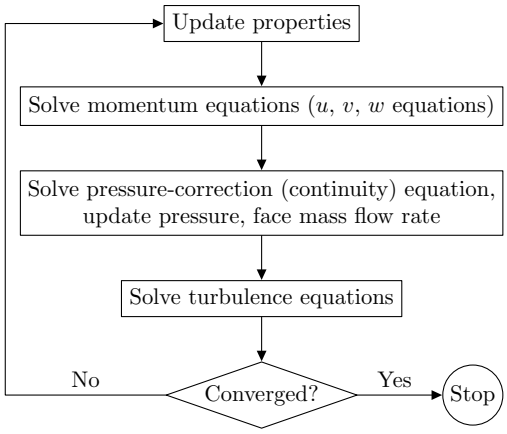

Figure 2. The segregated algorithm process

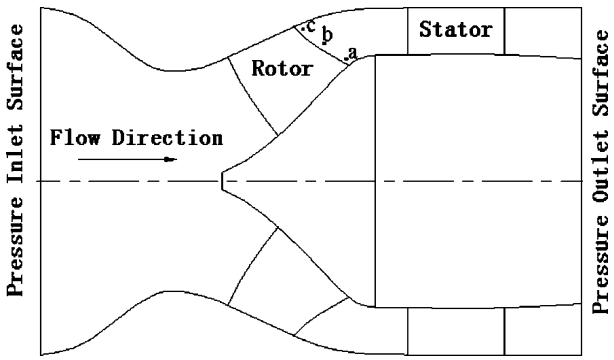

Figure 3. Meridian view of the computational domain and the inspected position of the rotor's wake

to 100 mm downstream of the stator's trailing edge. A meridian view of the computational domain is shown in Figure 3.

The computational domain has been divided into three zones. The first zone is the pressure inlet region upstream of the rotor. The second is the rotor flow passage and the adjacent region. The third is the stator flow passage and the downstream area.

Various types of grids were used in these zones. Detailed grid information on several basic surfaces is shown in Table 2. A grid example of the rotor surface is shown in Figure 4. The surface between the adjacent zones is defined as an internal surface and the zones share grid nodes. The grid numbers in the three zones are 107 337, 941 625 and 1 052 097, respectively. The total grid number of the whole computational domain is 2 101 059.

5. Boundary conditions

The gauge inlet total pressure, turbulence intensity and hydraulic diameter are defined as boundary conditions at the pressure inlet surface. The outlet static pressure, backflow turbulence intensity and backflow turbulence viscosity ratio are specified as boundary conditions at the pressure outlet surface. The treatment of

Table 2. Grid details on several basic surfaces

Surface	Grid type	Grid number
Rotor P.S	Quadrilateral	45×31 in axial and spanwise direction
Rotor S.S	Quadrilateral	45×31 in axial and spanwise direction
Stator P.S	Quadrilateral	37×16 in axial and spanwise direction
Stator S.S	Quadrilateral	37×16 in axial and spanwise direction
Rotor Hub Surf.	Triangle	22 390
Stator Hub Surf.	Triangle	38 242
Rotor Casing Surf.	Triangle	33 646
Stator Casing Surf.	Triangle	46 270

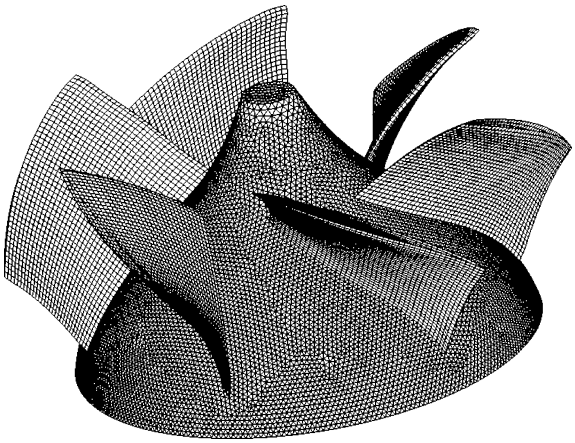

Figure 4. Computational grid on the rotor surface

a stationary/rotating part utilizes a multiple reference frame technique. The rotor hub and blades are specified as fixed walls in a rotating frame of reference. Its rotary speed is 1 800 rpm. In addition, the rotor casing is a counter-rotating wall (a stationary wall in the fixed frame of reference). The stator and its walls are defined as a stationary wall. Periodic boundary conditions have not been used when calculating the whole diagonal rotor in this study.

6. Results and discussion

6.1. Validation of the present work

In order to validate the present code and numerical method, the calculated aerodynamic characteristic curve of the rotor has been compared with the published experimental results [7]. As shown in Figure 5, the calculated values are in agreement with the earlier experimental data, which shows that the present numerical method is acceptable and reliable. The focus of this study has been the flow phenomena at the designed flow rate: the flow coefficient, φ , is equal to 0.563; the total pressure coefficient, ψ, is equal to 0.75.

As shown in Figure 6, the calculated streamline distribution on the meridian surface is consistent with the design value, which proves that the streamline curvature method used in our study is practical.

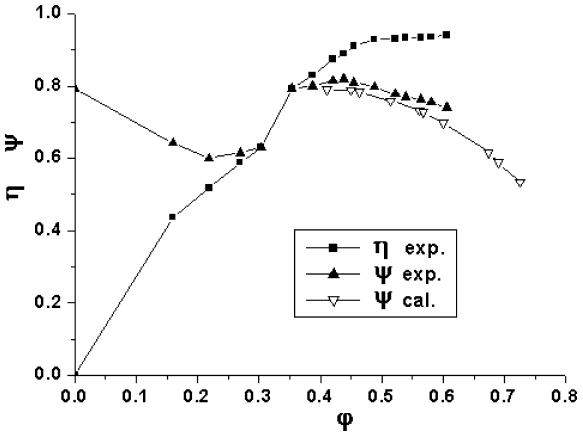

Figure 5. Aerodynamic characteristic curve

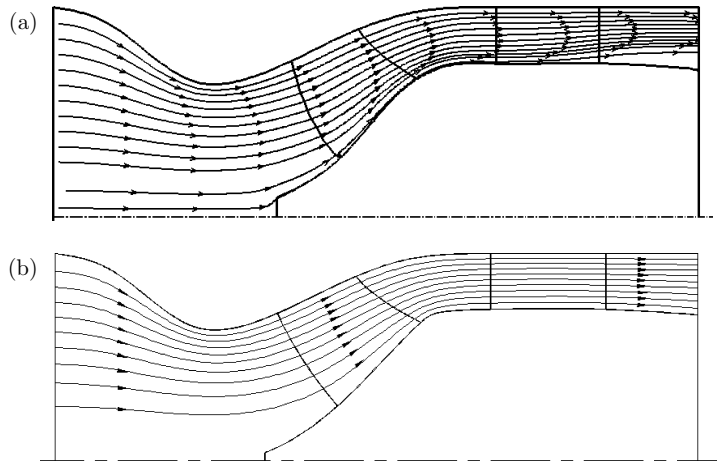

Figure 6. Streamline distribution on meridian surface:
(a) calculated value; (b) design value by SCM method

6.2. Meridian velocity distribution

The meridian velocity distribution upstream and downstream of the diagonal rotor has been analyzed and are presented in Figures 7 and 8, respectively. In these figures, the abscissa represents the non-dimensional distance from the hub wall to the casing wall. The solid squares denote the design values of the SCM method. The solid triangle symbol denotes the calculated results from the present study, while the inverted blank triangle symbol represents experimental data [7]. Meridian velocity has been normalized by the tangential velocity at the rotor exit, U_t. As shown in Figures 7 and 8, upstream of the rotor meridian velocity increases gradually from the hub wall to the casing wall. At the same time, downstream of the rotor meridian velocity decreases from the hub wall to the casing wall. This decrease is sudden and mainly caused by the end-wall boundary layer. The boundary layer of the casing wall occupies nearly 10% of the flow passage. Both figures show that the meridian velocity distribution is in agreement with the design values and experimental data,

except for a small difference noted near the hub and the casing wall downstream of rotor. As our data are further proof of the validity of the present numerical methods, these applications may be used to design and analyze swept diagonal rotors in future studies.

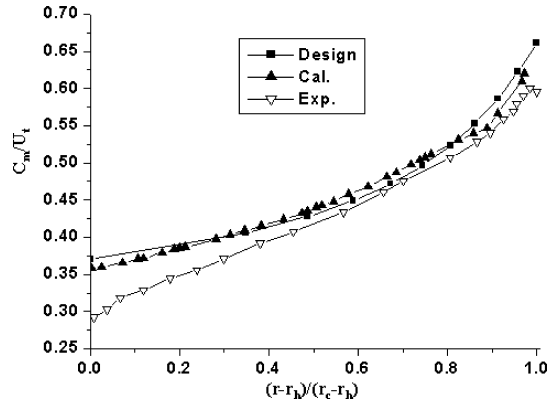

Figure 7. Meridian velocity distribution along spanwise direction upstream of the rotor

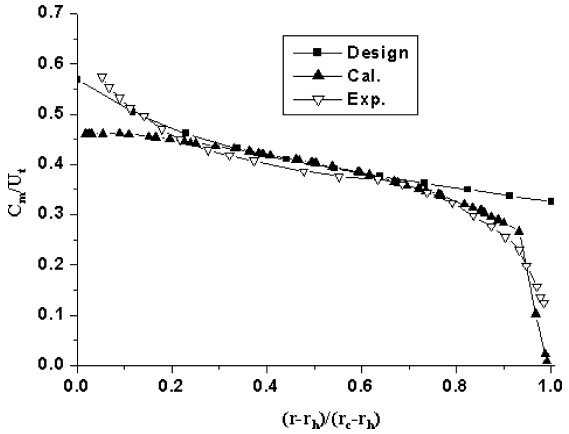

Figure 8. Meridian velocity distribution along spanwise direction downstream of rotor

6.3. Pressure distribution on the rotor and stator surface

Figure 9 presents the static pressure distribution at various heights along the rotor blade surface. Static pressure increased gradually from the rotor's leading edge to the trailing edge as shaft power was converted into flow momentum by the rotor. On the rotor pressure surface, static pressure increased gradually along the height of a blade. However, on the rotor suction surface, static pressure exhibited a different variation trend (Figure 9). In the front a gradual decrease was found in 60% of the chord region from the hub to the casing. In the back, an increase was noted along the height of the blade in 40% of the chord region. Furthermore, the isoline distribution of static pressure on the rotor surface clearly revealed this characteristic. The maximal static pressure on the rotor pressure surface was located at the tip end-wall region near the rotor's trailing edge (see Figure 10).

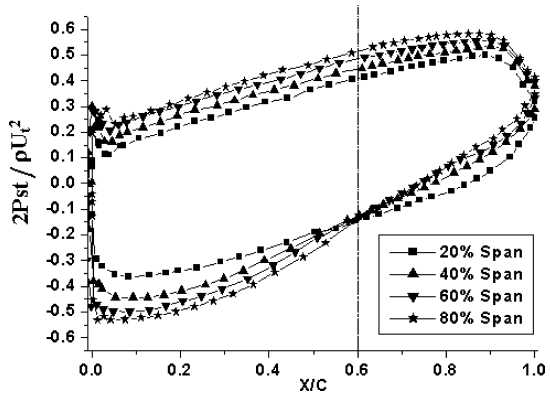

Figure 9. Static pressure distribution at various spanwise sections on the rotor surface

Figure 11 shows the static pressure distribution at various heights along the stator blade surface. Static pressure increased gradually from the stator's leading edge to the trailing edge. This indicates that dynamic pressure was gradually converted by the stator to static pressure. Both on the stator's suction and pressure surface, static pressure varied along the height of a blade.

6.4. Wake flow downstream of the rotor

Rotor wake is an important source of loss in turbo-machinery. If the rotor wake were not thoroughly decayed subsequent to entering the stator flow passage, it would bring about considerable loss and worsen the flow in the stator passage [11, 12]. An analysis of the variation of axial velocity along the circumferential direction can capture rotor wake. In general, a sudden reduction in axial velocity downstream of the rotor indicates the presence of rotor wake or a combination of all vortices which occurred upstream of the rotor's trailing edge.

In order to study rotor wake characteristics along the height of a rotor blade, the variation of axial velocity along various circumferences downstream of the rotor has been investigated. The inspected circumferential positions are marked as points **a** to **c** in Figure 3. The inspected positions are 5mm downstream of the rotor's trailing edge and their axial velocity distributions along the circumference are shown in Figure 12. A highly reduced axial velocity distribution at three circumferential positions (-40°, 20°, 80°) can be seen in Figure 12. It indicates the presence of rotor wake at the above-mentioned circumferential positions.

The reduction in axial velocity near the hub and the casing end-wall was greater than that observed in the midspan region, which means that the rotor's wake near the hub (Figure 12a) and the casing wall (Figure 12c) was stronger than that in the midspan region (Figure 12b). This shows that the hub and the casing end-wall influence the wake.

Figure 13 shows axial velocity distributions along the midspan circumference (point **b** in Figure 3) at a different flow rate. The maximum reduction of axial velocity occurred at the lower flow rate ($\varphi = 0.437$), which indicates that rotor wake at a lower flow rate ($\varphi = 0.437$) is stronger than that at a higher flow rate ($\varphi = 0.675$).

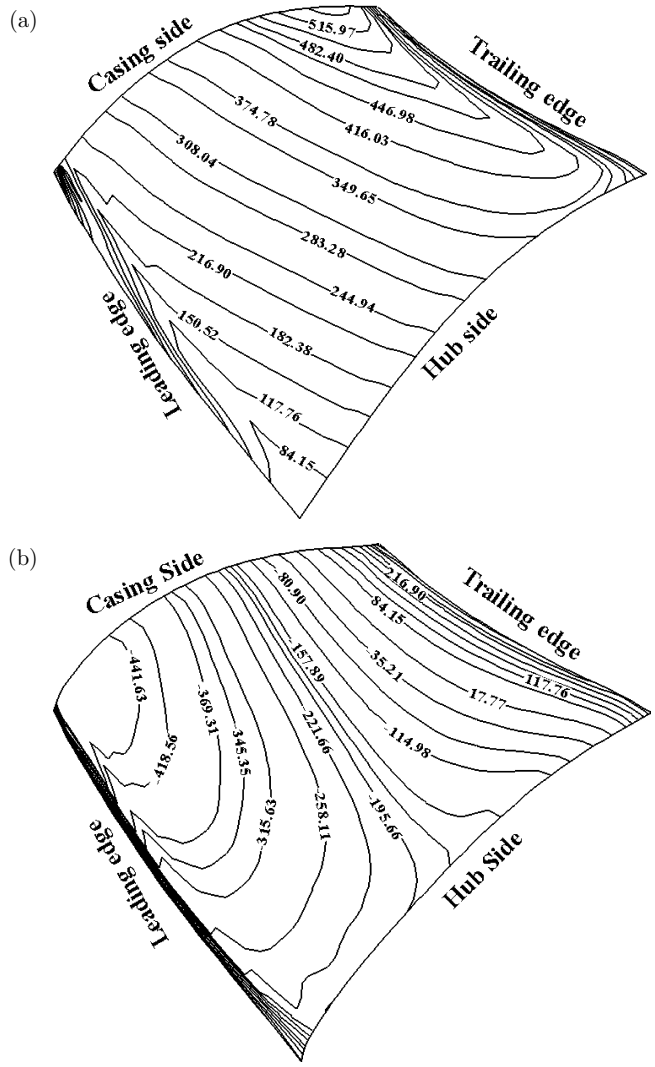

Figure 10. The isoline distribution of static pressure on the rotor surface: (a) rotor pressure surface; (b) rotor suction surface

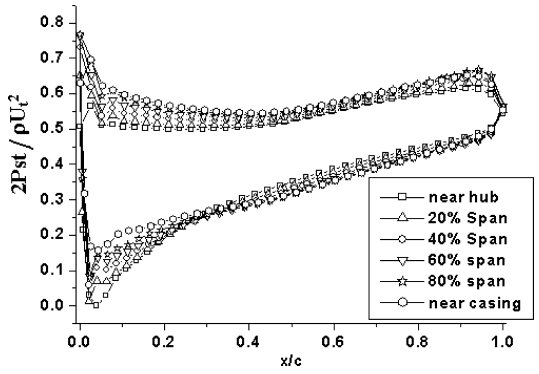

Figure 11. Static pressure distribution at various spanwise sections on the stator surface

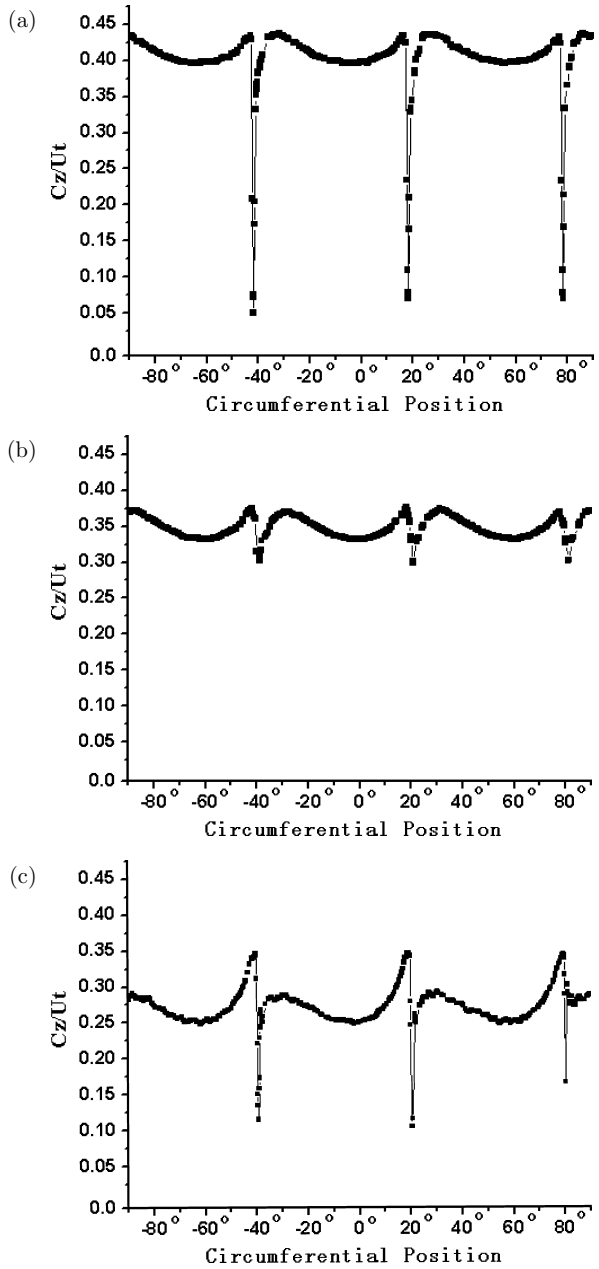

Figure 12. Axial velocity distribution along different circumferences 5mm downstream of rotor: (a) circumference 5mm above the hub wall; (b) midspan circumference; (c) circumference 5mm below the casing wall

6.5. Passage vortex in the stator flow passage

A great portion of the losses found in turbomachinery is due to the passage vortex. The inlet boundary layer and the boundary layers on the hub and tip endwalls are the main components of the passage vortex [13, 14]. To study the passage vortex in the stator flow passage, secondary vectors at various axial chord planes of

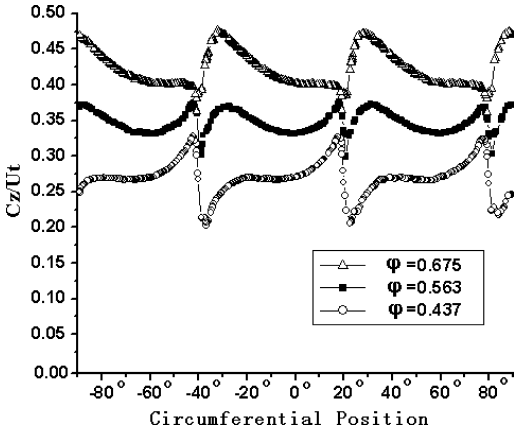

Figure 13. Axial velocity distribution along midspan circumference (5mm downstream of rotor) at different flow rates

the stator were used (see Figure 14). Figure 14 shows the generation and development of a secondary flow vortex in the stator flow passage.

Seen in the front section of the stator flow passage located 60% before the axial chord plane of the stator, the passage vortex had not formed yet (Figure 14a). Secondary vectors mainly flowed from the stator suction surface to the pressure surface. Near the hub wall regions, due to the influence of the hub wall boundary layer, secondary vectors were very small. The passage vortex was clearly formed at 80% of the axial chord plane of the stator, near the hub end wall. The passage vortex was a consequence of the hub boundary layer and deflection of the flow in the stator passage. The vortex was clockwise and clearly visible, even though secondary vectors near the hub wall were very small. The vectors flowed from the stator pressure surface to the suction surface (Figure 14b). This passage vortex continued to develop until the exit of the stator passage. It developed into a large passage vortex that was almost centered at the midspan at 99% of the axial chord plane of the stator (see Figure 14c). This resulted in a high spanwise flow at this plane. The flow was toward the midspan near the stator suction surface and toward the hub end-wall near the stator pressure surface. These flow phenomena were in accordance with the pressure distribution on the stator pressure surface (see Figure 11), where static pressure gradually increased from the hub to the casing.

7. Conclusions

Flow phenomena in a diagonal rotor has been analyzed in the present study using the Reynolds-averaged Navier-Stokes equations coupled with the k-ε turbulence model. The following conclusions can be drawn from the presented results:

1. Upstream of the rotor meridian velocity gradually increases along the height of a rotor blade, while downstream of the rotor meridian velocity gradually decreases from the hub to the casing. The casing wall boundary layer occupies almost 10% of the flow passage downstream of the rotor.
2. On the rotor pressure surface, static pressure gradually increases from the hub to the casing. On the rotor suction surface along the spanwise direction, static

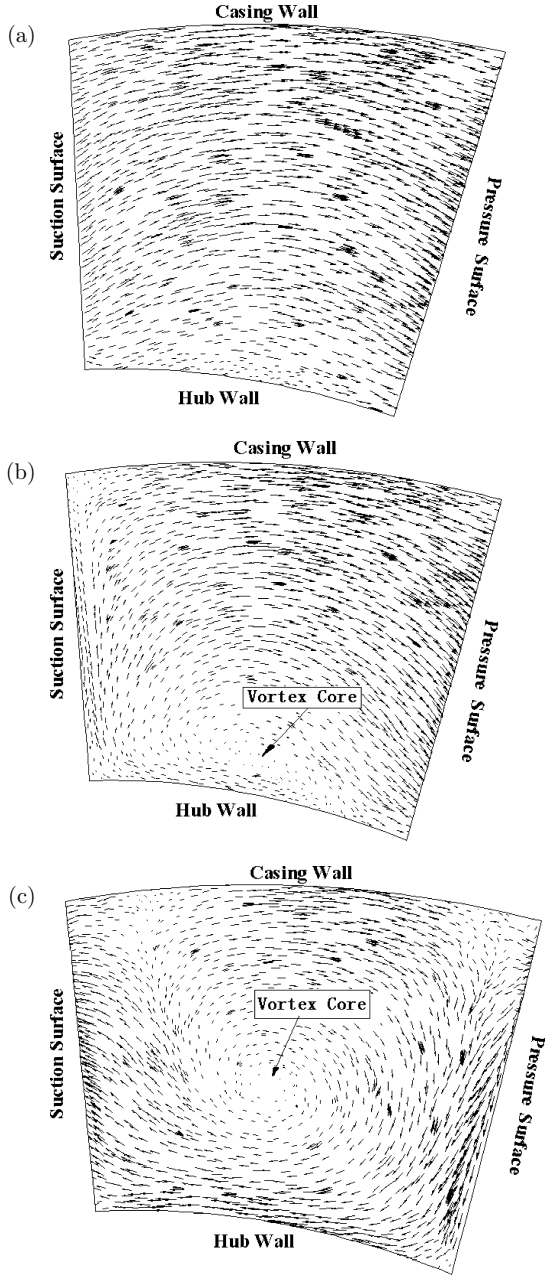

Figure 14. Secondary velocity vectors distribution at different axial chord plane of the stator: (a) 60% of the axial chord plane of the stator; (b) 80% of the axial chord plane of the stator; (c) 99% of the axial chord plane of the stator

pressure gradually decreases in the front section of 60% of the axial chord region, and increases 40% in the back axial chord region.

3. Due to the influence of the end-wall boundary layer, rotor wake near the hub and the casing wall is stronger than that in the midspan region. Rotor wake at a lower flow rate is stronger than that at a higher flow rate.

4. The stator passage vortex forms at 80% of the axial chord plane of the stator and is located near the hub end-wall. It continues to develop until the exit of the stator passage and is centered at the midspan at 99% of the axial chord plane of the stator.

Acknowledgements

The present research has been supported by the Chinese National Foundation of Natural Sciences (under Contract No. 50176012).

References

[1] Wennerstorm A J 1990 *ASME J. Turbomachinery* **112** 567
[2] Wadia A R, Szucs P N and Crall D W 1998 *ASME J. Turbomachinery* **120** 671
[3] Sasaki T and Breugelmans F 1998 *ASME J. Turbomachinery* **120** 454
[4] Beller M G and Carolus T H 1999 *ASME J. Turbomachinery* **121** 59
[5] Inoue M 1997 *Proc. 5th Int. Conf. Fluid Machinery*, Seoul, Korea, pp. 117–131
[6] Wu C H 1952 *ASME Paper* No. 50-A-79, *Trans. ASME* Nov. 952 or NACA TN 2604
[7] Inoue M and Wu K C 1984 *Proc. China-Japan Joint Conf. Hydraulic Machinery and Equipment*, Hangzhou, China, pp. 21–30
[8] Inoue M 1979 *Bulletin of JSME* **9** 1190
[9] Pantankar S V and Spatding D B 1972 *Int. J. Heat and Mass Transfer* **15** 37
[10] Pantankar S V 1980 *Numerical Heat Transfer and Fluid Flow*, Mc Graw-Hill
[11] Kerrebrock J L and Mikołajczak A A 1970 *ASME J. Eng. Power* **15** 359
[12] Dale E Z, John J A, Anthony J S and Theodore H O 2002 *ASME J. Turbomachinery* **124** 275
[13] Chen N X, Wang Z Q, Wang S T and Feng Guotai 2001 *Proc. 5th Int. Symp. Experimental and Computational Aerothermodynamics of Internal Flows*, Gdansk, Poland, pp. 19–42
[14] Fiedrichs J, Baumgarten S, Kosyna G and Stark U 2001 *ASME J. Turbomachinery* **123** 483